PHYSICS OF FLUIDS **22**, 095102 (2010)

Effect of the Prandtl number on a stratified turbulent wake

Matthew B. de Stadler,[1] Sutanu Sarkar,[1,a)] and Kyle A. Brucker[2,b)]
[1]University of California San Diego, La Jolla, California 92093, USA
[2]Naval Hydrodynamics Division, Science Applications International Corporation,
San Diego, California 92121, USA

(Received 23 January 2010; accepted 30 June 2010; published online 15 September 2010)

Direct numerical simulation is employed to study the effect of the Prandtl number, $\mathrm{Pr}=\nu/\alpha$ with ν the molecular viscosity and α the molecular diffusivity, on a turbulent wake in a stratified fluid. Simulations were conducted at a Reynolds number of 10 000, $\mathrm{Re}=UD/\nu$ with U the velocity of the body and D the diameter of the body, for a range of Prandtl numbers: 0.2, 1, and 7. The simulations were run from $x/D=6$ to $x/D=1200$, a range that encompasses the near, intermediate, and far wake. Mean quantities such as wake dimensions and defect velocity were found to be weakly affected by Prandtl number, the same result was observed for vorticity as well. The Prandtl number has a strong effect on the density perturbation field and this results in a number of differences in quantities such as the total energy of the wake, wave flux, scalar and turbulent dissipation, mixing efficiency, spectral distribution of energy in the density and velocity fields, and the transfer of energy between kinetic and potential modes. The approximation $\mathrm{Pr}=1$ for the ocean is often used in practice. As the qualitative behavior of the large-scale features was the same for the three cases, we conclude that $\mathrm{Pr}=1$ is a reasonable approximation for the $\mathrm{Pr}=7$ case in stratified wake simulations, given the significantly higher computational cost required at large Prandtl number. [doi:10.1063/1.3478841]

I. INTRODUCTION

Direct numerical simulation (DNS) is employed to study the effect of the Prandtl number, $\mathrm{Pr}=\nu/\alpha$ with ν the molecular viscosity and α the molecular diffusivity, on a turbulent wake in a stratified fluid. Historically, stratified wake simulations have been performed at $\mathrm{Pr}=1$ although $\mathrm{Pr}=7$ for thermally stratified water and $\mathrm{Pr}=700$ for salt stratified water. The reason is the high numerical cost, proportional to Pr^2 for three-dimensional simulations with explicit time integration, of simulating larger values of Pr.

For DNS it is necessary to resolve all scales of motion. Assuming that density behaves as a passive scalar, the Batchelor length scale η_B is related to the Kolmogorov length scale η by the relation $\eta_B=\eta/\sqrt{\mathrm{Pr}}$ for large Pr.[1] While the density is not a passive scalar, a first approximation for the necessary resolution can be made using the estimate for a passive scalar. The requirement of increased resolution in each of the three spatial dimensions results in an additional reduction of the timestep due to the Courant–Friedrichs–Lewy condition for stability. As an example of the high cost of simulating large values of Pr, the $\mathrm{Pr}=7$ DNS at a modest Reynolds number, $\mathrm{Re}=UD/\nu$ with U the velocity of the body and D the diameter of the body, of $\mathrm{Re}=10\,000$ performed here requires approximately 1.88×10^9 grid points.

It is *assumed* that the Prandtl number makes only a small difference in the behavior of the wake. It is well known that increasing Pr increases the dynamic range of scalar fluctuations but it is not known how the Prandtl number affects the coupling of density, an active scalar, to the velocity field and consequently impacts the dynamics of the wake. The assessment of the Pr effect takes urgency given the recent results of Brucker and Sarkar[2] who found that increasing the Reynolds number by a factor of 5 caused large qualitative and quantitative changes in wake behavior.

A. Previous research

The towed wake in a stratified fluid is a problem which has received much attention from both experimental and numerical studies. Research up to 1979 was primarily experimental, a comprehensive review is given by Lin and Pao.[3] It has been commonly accepted that there are three major regions that characterize the towed wake. The first region is the near wake where the wake develops in an unstratified manner. The second region, referred to as the nonequilibrium (NEQ) regime following Spedding,[4] is characterized by the effect of stratification which causes an initial collapse as the potential energy associated with the wake can no longer be sustained by the decaying kinetic energy of the wake. Stored potential energy in the density field causes the wake to collapse vertically and spread horizontally. The initial collapse results in a dynamic exchange between kinetic and potential energy as the wake decays downstream. This exchange generates strong internal wave activity which radiates energy from the wake region to the ambient background. The third region, referred to as the Q2D region, occurs at late time when stratification has confined the wake to quasi-two-dimensional horizontal motion. This region is characterized by large-scale, high aspect ratio vortex structures.

In addition to the three major regions discussed above, Bonnier and Eiff[5] propose considering the first collapse region as separate from the NEQ region. A recent DNS by

---

[a)] Electronic mail: sarkar@ucsd.edu.
[b)] Formerly at University of California San Diego.

1070-6631/2010/22(9)/095102/15/$30.00

Brucker and Sarkar[2] at Re=50 000 showed the existence of a different scaling region at the end of the NEQ region. Diamessis and Spedding[26] found similar results in their high Re numerical simulations.

Previous simulations[2,6,7,26] have shown that simulations initiated with a mean profile with superimposed fluctuations, but no body, have proven successful in capturing the dynamics of towed wakes in the intermediate and far wake. Gourlay *et al.*[6] found that coherent vortices formed at late time, independent of stratification or seeding in the early wake. They concluded that the late time vortex structures are due to the initial vorticity distribution of the mean flow.

To the best of the authors' knowledge, this paper is the first study of the effect of the Prandtl number on the turbulent stratified wake. Previous research concerning the effect of the Prandtl number on different classes of turbulent flows has been performed and conclusions from those studies are summarized as follows. Gerz, Schumann, and Elghobashi[8] found that high frequency components of the countergradient heat flux cause an increase in the dissipation rate for kinetic energy while causing a decrease in the dissipation rate of potential energy. Gerz and Yamazaki[9] found that higher Prandtl numbers increase the turbulent kinetic energy due to less potential energy being dissipated in the thermal field in their work on buoyancy-driven flows. In contrast to their previous work,[8] Gerz and Schumann[10] found that the Prandtl number influences the dissipation rate of available potential energy but not of kinetic energy for homogeneous shear flow turbulence with stratification. This different conclusion gives the appearance that the effect of the Prandtl number on shear flows is not fully understood; this contradiction will be examined later in Sec. III B. Smyth and Moum[11] found that, for a given Reynolds number, higher Prandtl number flows tend to be more isotropic than lower Prandtl number flows in their studies of stably stratified mixing layers. Smyth, Moum, and Caldwell[12] also found that the mixing efficiency decreases with increasing Prandtl number. In numerical simulations of stably stratified open channel flows, Wang and Lu[13] found that the Prandtl number has a significant impact on the structure of turbulent fluctuations, with smaller scale features appearing as Prandtl number increases. Lienhard and Van Atta[14] summarize previous results while contrasting their results for decaying grid turbulence in a stratified fluid. They found that the scalar variance is weakly affected by dissipation for high Pr fluids and that the evolution of scalar variance is more affected by the appearance of large-scale buoyancy forces. They also found that turbulent scalars exhibit significant fluctuations at high wavenumbers for large Pr. Scalar fluctuations are found to persist for much longer time than velocity fluctuations for higher Pr cases. Brucker and Sarkar[15] found that the bulk Richardson number decreases with increasing Prandtl number during the evolution of a shear layer. They also found that the root mean square (rms) velocity at the centerline decreases with increasing Pr. Consistent with Smyth, Moum, and Caldwell,[12] Brucker and Sarkar[2] found that the mixing efficiency decreases with increasing Pr.

B. Objectives

The present numerical simulations were designed to systematically investigate the effect of Prandtl number on a turbulent stratified wake. The effect of Prandtl number on the towed wake is of interest because the towed wake is a high Reynolds number shear flow and it is a problem of practical interest for bodies moving in the littoral region of the ocean. The study was conducted at a Reynolds number of 10 000 for a range of Prandtl numbers: 0.2, 1, and 7. A Froude number, $\mathrm{Fr}=U/(N^{*}D)$ where N^{*} denotes the constant initial value of the dimensional buoyancy (Brunt–Väisälä) frequency, of 2 was used. The Reynolds and Froude numbers were chosen so that both numerical and experimental data would be available for comparison. Most stratified turbulent wake simulations are conducted using Pr=1, that value was chosen as a baseline case. Pr=7 is a reasonable value for thermally stratified water. Pr=0.2 was chosen to have a test case with a low Prandtl number. The simulations were run from $x/D=6$ to $x/D=1200$, a range that encompasses the near, intermediate, and far wake. Areas of interest for this study on the effect of the Prandtl number are (i) the evolution of mean velocity and wake dimensions, (ii) the integrated mean kinetic energy (MKE), integrated turbulent kinetic energy (TKE), integrated turbulent potential energy (TPE), and their corresponding budgets, (iii) mixing efficiency, (iv) vortex dynamics, (v) internal wave flux, and (vi) spectra.

We are also interested in testing the assumption that it is reasonable to simulate towed bodies in the ocean using Pr =1. While a simulation using the Prandtl number of the ocean is prohibitively expensive, significant differences obtained with a moderate increase in Prandtl number would invalidate the assumption that Pr=1 is a reasonable approximation for bodies moving in the ocean. No simulations were performed for self-propelled wakes but it is anticipated that the Prandtl number effect in the towed case would also apply for the self-propelled case.

The organization of this paper is as follows. Section II contains the formulation and description of the simulations performed for this study, Sec. III discusses the similarities and differences in the wake at different Prandtl numbers, and Sec. IV presents conclusions.

II. FORMULATION

The formulation presented in this paper is based on the one used by Brucker and Sarkar[2] who simulated stratified wakes assuming Pr=1. Whenever possible, identical notation is used.

A. Model

The problem being examined is the towed wake behind a bluff body in a stratified fluid. The body is taken to be a rigid sphere of diameter D which is towed at a constant speed of U. Due to the high cost of simulating the far wake in a spatially evolving frame, the similar problem in a temporally evolving frame is simulated. In this frame, the streamwise direction is periodic and all statistics are therefore functions of (x_2,x_3,t). Statistics in the temporally evolving frame can

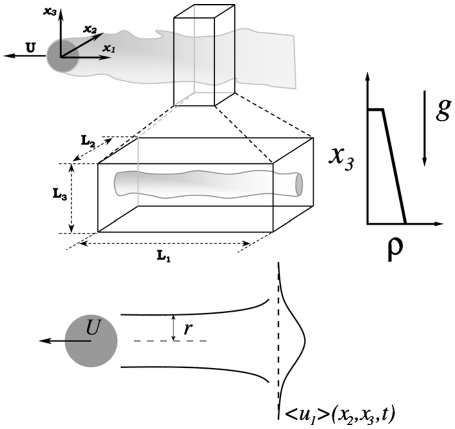

FIG. 1. Problem definition. Note that simulations are performed in the temporally evolving frame shown on the left.

be related to the spatially evolving frame by the relationship $x=Ut$, where x is the distance behind the body in the streamwise direction and t is the elapsed time in the temporally evolving simulation. The temporal approximation has been applied for many simulations of free shear flows.[2] The problem setup for this paper is shown schematically in Fig. 1.

The three-dimensional, unsteady, incompressible Navier–Stokes equations are solved numerically using DNS in the computational test section shown in Fig. 1. No turbulence models are used and all relevant velocity and density length scales are resolved.

B. Governing equations

The governing equations for this model are the incompressible unsteady Navier–Stokes equations subject to the Boussinesq approximation. Note that * is used to denote a dimensional quantity in the following presentation.

Mass:

$$\frac{\partial u_k^*}{\partial x_k^*}=0. \tag{1}$$

Momentum:

$$\frac{\partial u_i^*}{\partial t^*}+\frac{\partial(u_k^* u_i^*)}{\partial x_k^*}=-\frac{1}{\rho_0}\frac{\partial \tilde{p}^*}{\partial x_i^*}+\nu\frac{\partial^2 u_i^*}{\partial x_k^*\,\partial x_k^*}-\frac{\tilde{\rho}^*}{\rho_0}g\,\delta_{i3}. \tag{2}$$

Density:

$$\frac{\partial \rho^*}{\partial t^*}+\frac{\partial(u_k^*\rho^*)}{\partial x_k^*}=\alpha\frac{\partial^2\rho^*}{\partial x_k^*\,\partial x_k^*}. \tag{3}$$

Here ρ_0 is the reference density, ν is the dynamic viscosity, g is the magnitude of gravity, α is the molecular diffusivity, δ_{ij} is the Kronecker delta, $\tilde{p}^*$ is the deviation from hydrostatic pressure, and $\tilde{\rho}^*$ is the deviation of the density from the instantaneous mean background state, $\rho_0+\bar{\rho}^*(x_3,t)$. Note that the density has been decomposed as follows:

$$\rho^*(x_i,t)=\rho_0+\bar{\rho}^*(x_3,t)+\tilde{\rho}^*(x_i,t),$$

where $\tilde{\rho}^*(x_i,t)\ll\rho_0+\bar{\rho}^*(x_3,t)$. Equations (1)–(3) are nondimensionalized using the diameter of the sphere D, body velocity U, initial background density gradient $\Delta\rho=D|d\bar{\rho}^*/dx_3^*|(t=0)$, and the reference density ρ_0 as follows:

$$t=\frac{t^*U}{D},\quad x_i=\frac{x_i^*}{D},\quad u_i=\frac{u_i^*}{U},\quad \tilde{\rho}=\frac{\tilde{\rho}^*}{\Delta\rho},\quad p=\frac{\tilde{p}^*}{\rho_0 U^2}. \tag{4}$$

Upon substitution of the relations of Eq. (4) into Eqs. (1)–(3), the following nondimensional governing equations are obtained.

Mass:

$$\frac{\partial u_k}{\partial x_k}=0. \tag{5}$$

Momentum:

$$\frac{\partial u_i}{\partial t}+\frac{\partial(u_k u_i)}{\partial x_k}=-\frac{\partial p}{\partial x_i}+\frac{1}{\mathrm{Re}}\frac{\partial^2 u_i}{\partial x_k\,\partial x_k}-\frac{1}{\mathrm{Fr}^2}\tilde{\rho}\delta_{i3}. \tag{6}$$

Density:

$$\frac{\partial \rho}{\partial t}+\frac{\partial(u_k\rho)}{\partial x_k}=\frac{1}{\mathrm{Re}\ \mathrm{Pr}}\frac{\partial^2\rho}{\partial x_k\,\partial x_k}. \tag{7}$$

Here $\mathrm{Re}=(UD)/\nu$ is the Reynolds number, $\mathrm{Pr}=\nu/\alpha$ is the Prandtl number, and $\mathrm{Fr}=U/(N^*D)$ is the Froude number with N^* denoting the constant initial value of the dimensional buoyancy (Brunt–Väisälä) frequency. The nondimensional buoyancy frequency is $N\equiv\mathrm{Fr}^{-1}$. Unless otherwise noted, all variables to follow in the paper are expressed in nondimensional form.

C. Reynolds decomposition

For analyzing data, the Reynolds decomposition is used to write each variable as the combination of a mean and small fluctuating component as follows:

$$u_i=\langle u_i\rangle+u_i',\quad \rho=\langle\rho\rangle+\rho',\quad p=\langle p\rangle+p',$$

where angled brackets refer to an average over the entire homogeneous periodic direction x_1. Note that quantities such as $\langle u_i\rangle$ are functions of (x_2,x_3,t). To quantify the fluctuating quantities it is necessary to employ root mean square averaging using the following formula: $\phi_{\mathrm{rms}}=\sqrt{\langle(\phi-\langle\phi\rangle)^2\rangle}$, where ϕ is the variable of interest. Note that the rms quantities are also functions of (x_2,x_3,t).

D. Numerical scheme

The numerical algorithm is similar to that discussed by Basak,[16] Basak and Sarkar,[17] and Brucker and Sarkar.[2,15] The numerical code of Brucker and Sarkar[2] was used with minor updates to allow for stretched grids. Validation of the numerical code, including a detailed comparison to existing

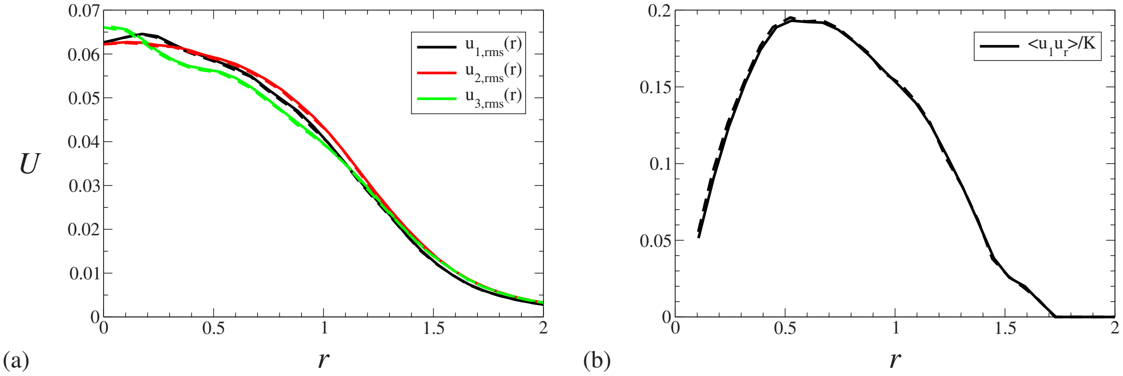

FIG. 2. (Color online) Spatial profiles after the adjustment procedure. (a) Root mean square profiles of the velocity. (b) Normalized Reynolds shear stress. The Pr=7 case is shown with a solid line and the Pr=1 and Pr=0.2 cases are represented with dashed lines. Note that $r=\sqrt{x_2^2+x_3^2}$.

experimental and numerical towed wake studies, is provided in Brucker and Sarkar,[2] see Figs. 6–8. A summary of the algorithm is provided here. A finite volume staggered-grid method is employed to solve the nondimensional Boussinesq form of the Navier–Stokes equations, Eqs. (5)–(7). Spatial derivatives are evaluated using second-order centered differences and the low-storage explicit third-order Runge–Kutta method of Williamson[18] is used for time advancement. To remove divergence, a pressure Poisson equation is solved using a parallel multigrid solver that employs an increasing number of relaxation sweeps during coarsening to accelerate convergence.

The main difference between the current numerical scheme and the one used by Brucker and Sarkar[2] is that the current simulations were performed with stretched grids in the x_2 and x_3 directions. Line Gauss–Seidel is used as the smoother in the parallel multigrid solver for the Poisson pressure equation. Lines are taken in the x_1 direction. The numerical treatment of the advective terms in Eqs. (6) and (7) is slightly different as well. For these terms a quasi-second-order discretization is used instead of a fully second-order discretization as the quasi-second-order discretization has better energy conserving properties.[19]

E. Initial conditions

The initial mean profile corresponds to the Gaussian profile used in previous towed wake cases,[2]

$$\langle u_i\rangle(r) = U_0 \exp^{(-1/2)(r/r_0)^2},$$

where $r=\sqrt{x_2^2+x_3^2}$, $U_0=0.11$ is the peak defect velocity, and $r_0=0.5$ is the initial wake radius. Divergence free fluctuations are added with an initial spectrum,

$$E(k) = \left(\frac{k}{k_0}\right)^4 \exp^{-2(k/k_0)^2},$$

where k_0 is taken to be 4. The fluctuating field is spatially limited using the following damping function:

$$g(r) = a\left(1+\frac{r^2}{r_0^2}\right)\exp^{(-1/2)(r/r_0)^2},$$

where $a=0.055$ is the maximum centerline amplitude of the velocity fluctuations. The velocity field is advanced for $t_{\text{adjust}}=7.05$ using the unstratified Navier–Stokes equations while holding the mean profile constant. This adjustment procedure[2] allows turbulence correlations to build up to realistic values while retaining a reasonable mean profile. The criterion that $\max(\langle u_1' u_r'\rangle/K)\sim 0.2$, where K is the turbulent kinetic energy defined by $K=\langle u_i' u_i'\rangle/2$, for turbulent shear flow was used to judge when to conclude the initial adjustment period. Implicit in this criterion is the assumption that the near wake is adjusted by shear before stratification can take effect. Density fluctuations were set to zero following Brucker and Sarkar.[2] The effect of nonzero density fluctuations was evaluated by Brucker and Sarkar[15] and Riley and de Bruyn Kops[20] for the case of a temporally evolving shear layer; both found almost identical results with or without initial density fluctuations.

The goal for this study is to vary the Prandtl number while holding all other parameters constant to minimize the degrees of freedom involved. Therefore, the initial velocity field is obtained on the fine grid used for the Pr=7 case and then interpolated onto the corresponding coarser grid used for simulating the Pr=0.2 and Pr=1 cases. The initial conditions used for the three simulations are shown in Fig. 2. Figure 2(a) shows the radial distribution of the rms velocity fluctuation components. Note that anisotropy is present in the initial conditions consistent with turbulent shear flows. Figure 2(b) shows the normalized Reynolds shear stress $\langle u_1' u_r'\rangle/K$ which was used to identify when reasonable cross-correlation had developed.

Following previous simulations,[2,7] the end of the adjustment period is taken to correspond to $t=6.0$ to match experimental data from Bevilaqua and Lykoudis[21] for an unstratified wake. During the first two time units of the simulations, $t=6$ to $t=8$, gravity is slowly ramped up from $g(t=6)=0$ to its full value using the relation $g(t)=g_0\tanh(1.5t/t_{\text{ramp}})$, where g_0 is the magnitude of gravity, t is the current time, and $t_{\text{ramp}}=2$ is the time over which gravity is adjusted. Gravity is slowly turned on so that the absence of initial density fluctuations will be corrected by the velocity fluctuations as the wake begins to feel the effect of stratification.

TABLE I. Simulation parameters. [Note that t_f and L_i are nondimensionalized following Eq. (4). t_f refers to the time at the end of the simulation. The lengths given above are all for the test domain. The computational domain for the simulations in x_2 and x_3 is larger as it includes a sponge region for enforcing the boundary conditions.]

Case	Re	Fr	Pr	t_f	L_1	L_2	L_3	n_1	n_2	n_3
Pr=7 early	10 000	2	7	296.7	59.98	26.02	13.43	3584	1024	512
Pr=7 late	10 000	2	7	1200	59.95	26.02	13.43	1280	512	256
Pr=1	10 000	2	1	1200	59.95	26.02	13.43	1280	512	256
Pr=0.2	10 000	2	0.2	1200	59.95	26.02	13.43	1280	512	256

F. Boundary conditions

A combination of Neumann and Dirichlet boundary conditions is applied at the x_2 and x_3 boundaries to represent the undisturbed background conditions far away from the wake,

$$\begin{gathered}\frac{\partial u_i}{\partial x_j}(\pm L_{2,3})=0,\quad \frac{\partial p}{\partial x_2}(\pm L_2)=0,\quad p(\pm L_3)=0,\\ \frac{\partial \rho}{\partial x_2}(\pm L_2)=0,\quad \frac{\partial \rho}{\partial x_3}(\pm L_3)=-\Delta\rho/D,\end{gathered}\tag{8}$$

where $i=1,2,3$ and $j=2,3$. In addition to the above boundary conditions, a sponge region taking the form of a Rayleigh damping function is used in the x_2 and x_3 directions to prevent reflection of outgoing waves and other extrusions into the computational test section. The Rayleigh damping function is added to the right hand side of Eqs. (6) and (7) as

$$-\phi(x_i)[U_i(x_i,t)-U_{i,\infty}],\qquad -\phi(x_i)[\rho(x_i,t)-\rho_\infty],\tag{9}$$

respectively, where $U_{i,\infty}(x_2,x_3)=[0,0,0]$ is the free stream velocity and $\rho_\infty(x_2,x_3)=\rho_0-(\Delta\rho/D)x_3$ is the free stream density. $\phi(x_i)$ increases quadratically from $\phi=0$ at the beginning of the sponge region to $\phi=A_i$ at the domain boundaries. The sponge is designed so that it is always sufficiently far away from the wake so that it does not interfere with the main flow. For all of the simulations, the sponge amplitude was set to $A_2=A_3=0.1$. In the Pr=7 case, 20 points were used for the sponge at each of the x_2 and x_3 boundaries over lengths of $L_{2,s}=1.85$ and $L_{3,s}=1.75$, respectively. For the Pr=0.2, Pr=1, and the second part of the Pr=7 cases, 20 points were used for the sponge at each of the x_2 and x_3 boundaries over lengths of $L_{2,s}=1.66$ and $L_{3,s}=2.50$, respectively.

G. Simulation parameters

The parameters used in the three cases are presented in Table I. The parameters used to generate the grids for the different cases are discussed in Sec. II G 1. The Pr=7 case, requiring a grid of approximately 1.88×10^9 grid points, is the most expensive of the three simulations because of the increased resolution needed to capture the Batchelor length scale. Due to the high cost of simulating a wake with Pr >1, the simulations were designed for a resolution of $\Delta x/\eta_L=4$, where η_L is the smallest length scale in the flow, either the Kolmogorov length scale or the Batchelor length scale depending on the value of Pr. While it would have been desirable to perform the simulations with $\Delta x/\eta_L=2$, our limited computing resources prevented this. The resolution is acceptable as in other studies, see review by Moin and Mahesh.[22]

To keep the cost of the Pr=7 case reasonable, a regridding procedure was used. This same procedure was also used by Brucker and Sarkar,[2] however the regridding was done at significantly later time for the current study. An overlap period was used to ensure that the errors introduced by the regridding process did not significantly affect the results.

The Pr=7 case required a total of approximately 14 000 hours of CPU time; the first part of the simultion took around 13 500 CPU hours using 448 processors and the second part took around 500 CPU hours using 40 processors. The Pr =0.2 and Pr=1 cases each used 40 processors and required approximately 800 hours of CPU time.

1. Computational grid

The computational grid was designed to use the fewest number of points possible while still retaining a high level of accuracy. The x_1 direction has uniform grid spacing. The x_2 and x_3 grids are comprised of three regions, as sketched in Fig. 3 and described below. The first region, a rectangle with $-l_2<x_2<l_2$ and $-l_3<x_3<l_3$, where l_i is the distance from the wake centerline in either x_2 or x_3, uses uniform grid spacing Δx. This region is where turbulence is expected to be most intense and where the greatest resolution is required.

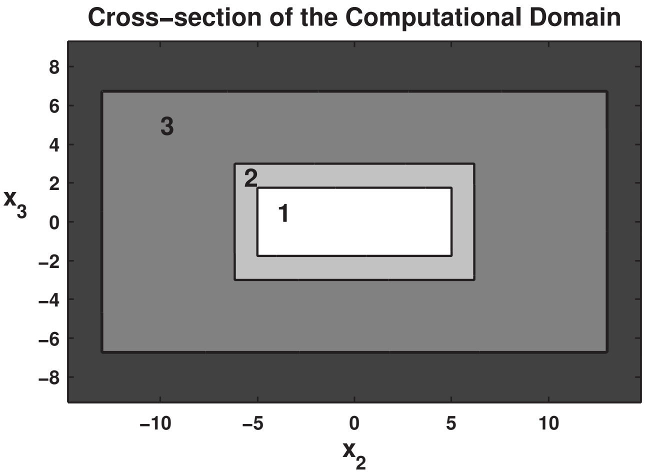

FIG. 3. A cross section of the computational domain in the nonperiodic directions. Section 1 is the region with constant grid spacing. The buffer region is denoted 2. Section 3 is the region with constant grid stretching. The outermost section is the sponge region.

TABLE II. Grid parameters.

Grid	l_2	l_3	$n_{i,b}$	min Δx	pc_2	pc_3
Pr=0.2,1,7 late	5.0	1.8	25	0.046 83	1.0049	1.0150
Pr=7 early	5.0	1.8	25	0.016 74	1.0092	1.0135

The middle region is a buffer zone that uses $n_{i,b}$ grid points to smoothly transition between the uniform grid of the center to the stretched grid in the outer region. The outer region uses a constant rate of stretching. The formula for the buffer region is

$$x_i(i+1) = x_i(i) + [x_i(i) - x_i(i-1)] \times \left\{ 1 + \tanh\left[4\left(\frac{2j - n_{i,b}}{n_{i,b}} \right) \right] \frac{(pc_i - 1)}{2} + \frac{pc_i - 1}{2} \right\}, \qquad (10)$$

$$j = 1, n_{i,b},$$

and for the outer region is

$$x_i(i+1) = x_i(i) + [x_i(i) - x_i(i-1)]pc_i, \qquad (11)$$

where j is an index that goes from unity at the edge of the uniform grid to $n_{i,b}$ at the edge of the stretched grid, and pc_i is the percent stretching expressed in decimal form (1% stretching corresponds to $pc_i = 1.01$). Most of the flow in the outer region of the domain comes from internal waves and similar structures which are exiting the domain. The resolution required to capture such phenomena is much less restrictive than the resolution needed at the turbulent core of the wake. Note that only two grids are used, one for the early time part of the Pr=7 run, and a second coarser one for the Pr=0.2, Pr=1, as well as the late time part of the Pr=7 cases. The parameters for the two grids are given in Table II.

III. SIMULATION RESULTS

This section is structured into two subsections: one on important similarities between the three cases and another discussing the important differences between the three cases. For the purpose of this paper, a quantity is considered to be weakly influenced by the Prandtl number if the quantity behaves qualitatively similar in the three cases and its value is within 10% among the three cases. Differences between the Pr=7 and Pr=1 cases are of special interest as they correspond to an approximation that is usually made for simulating towed bodies moving in the ocean.

A. Important similarities

We are interested in determining the effect of the Prandtl number on overall wake quantities such as the maximum defect velocity and the wake dimensions. Following Brucker and Sarkar,[2] a second spatial centered moment of the square of the mean streamwise velocity $\langle u_1 \rangle(x_2, x_3, t)$ was used to describe the dimensions of the wake. The exact definitions of the wake width R_2 and the wake height R_3 are as follows:

$$R_\alpha^2(t) = F \frac{\int_A (x_\alpha - x_\alpha^c)^2 \langle u_1 \rangle^2 dA}{\int_A \langle u_1 \rangle^2 dA},$$
$$x_\alpha^c(t) = \frac{\int_A x_\alpha \langle u_1 \rangle^2 dA}{\int_A \langle u_1 \rangle^2 dA}, \qquad (12)$$

where $\alpha = 2, 3$, A is taken to be over the area of the x_2-x_3 plane excluding the sponge region, and $F=2$ is an amplification factor that sets R_2 and R_3 to $r_0 = 0.5$ at the start of the simulation.

The wake dimensions were found to behave very similarly between the three different cases. Figure 4(a) shows the defect velocity for each of the three cases. All three cases follow the same qualitative trend: an initial decay followed by an increase due to the initial collapse in the vertical owing to buoyancy followed by the NEQ regime and later the Q2D regime. The quantitative values are different due to differences in the feedback from the density field, this is discussed further in Sec. III B. The wake width and height have some slight quantitative differences at intermediate to late times but the Pr=1 case is a reasonable approximation for the Pr =0.2 and Pr=7 cases.

The vorticity field is similar between the three cases. This was established by examination of instantaneous slices of plane normal components of vorticity on centerline cuts in all three directions. Figure 5, vertical vorticity on a horizontal centerplane, illustrates the similar evolution of vorticity among cases. Small quantitative differences exist but the qualitative agreement, including the number and location of vortex cores, is excellent.

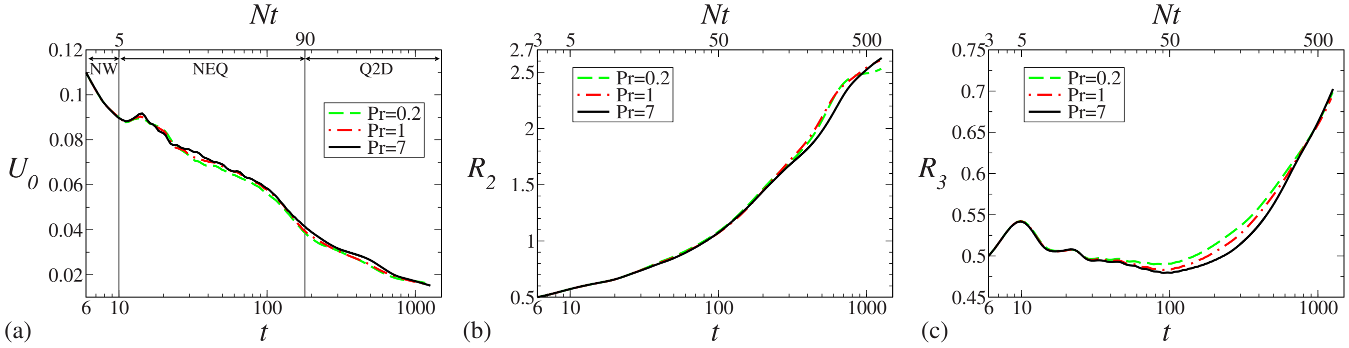

FIG. 4. (Color online) Overall wake quantities. (a) Defect velocity. (b) Wake width. (c) Wake height.

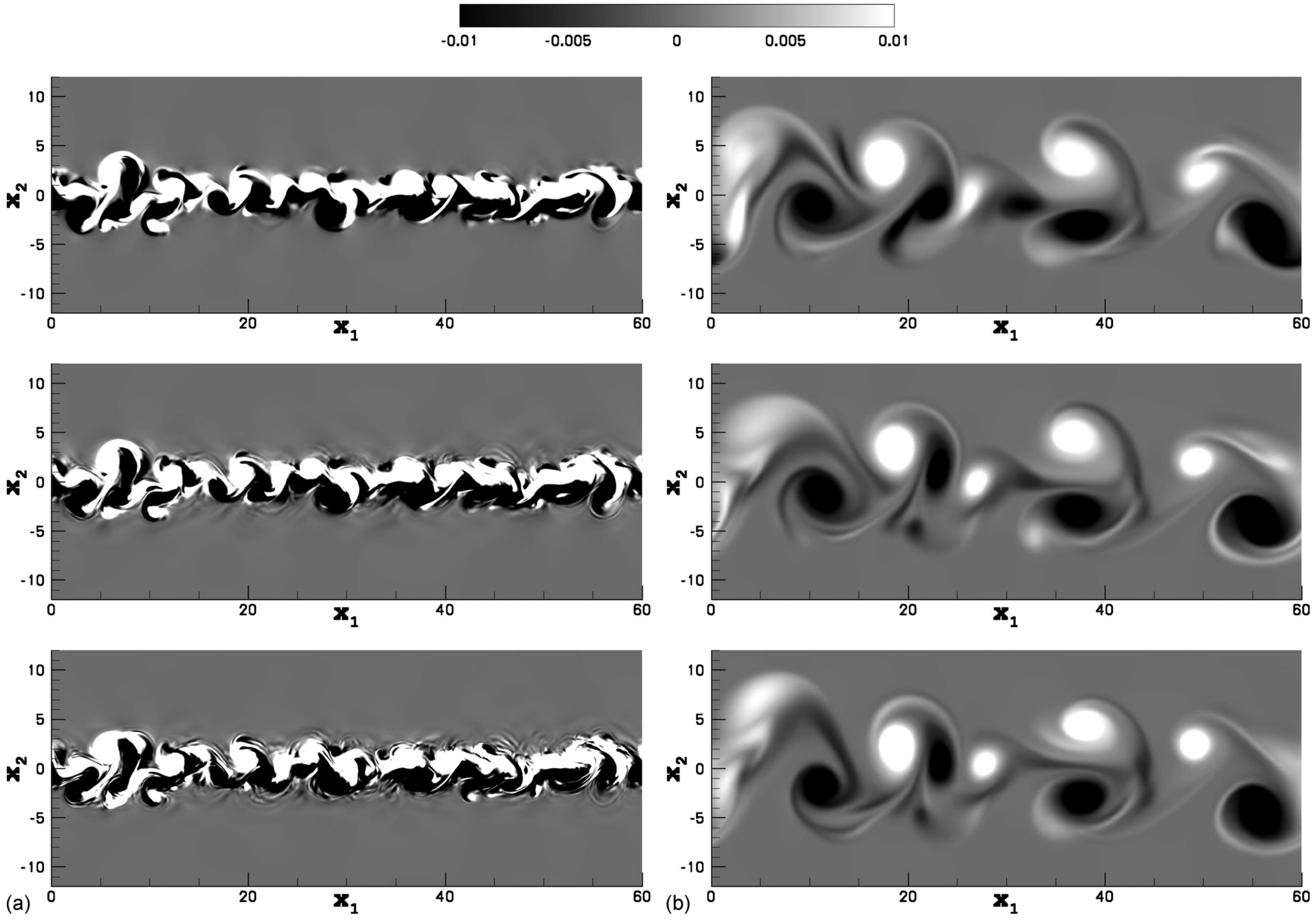

FIG. 5. Instantaneous ω_3 at the horizontal centerplane, $x_3=0$. Top Pr=0.2, middle Pr=1, bottom Pr=7. (a) ω_3 at $t=100$. (b) ω_3 at $t=1200$. Flow is from left to right.

Brucker and Sarkar[2] found that the mean kinetic energy is most strongly affected by the production of turbulent kinetic energy. As the production is a large-scale feature of the flow, the Prandtl number is not expected to strongly affect it. This implies that the mean kinetic energy will be very similar between the three cases and similarly the mean flow, which governs the defect velocity and wake dimensions, will also not vary significantly. This result was observed in the present simulations.

The wake dimensions, defect velocity, and vorticity fields are dominated by the mean flow which appears to be weakly influenced by the Prandtl number. These results agree well with the assumption that the Prandtl number makes a small difference in the behavior of the wake. Most of the differences due to Prandtl number appear in fluctuating quantities which are discussed in Sec. III B.

B. Important differences

The Prandtl number has a strong effect on the density field. Turbulence in the wake disturbs the density field by moving heavy fluid up and light fluid down which results in a rise in the potential energy of the wake. Buoyancy couples the potential energy stored in the density field to the kinetic energy of the velocity field. The Prandtl number governs the relative strength of diffusion in the velocity and density fields. Higher values of Pr correspond to lower molecular diffusivity which results in density fluctuations persisting for longer times. For lower values of Pr, the density fluctuations are damped more efficiently. The difference in the strength of the density fluctuations results in a number of differences in quantities such as the total energy of the wake, wave flux, scalar and turbulent dissipation, mixing efficiency, spectral distribution of energy in the density and velocity fields, and the transfer of energy between kinetic and potential modes. Each of these differences is discussed in this section.

The effect of Prandtl number on the density field can be seen by looking at contour plots of ρ' and ρ_{rms}. In agreement with Wang and Lu,[13] smaller scale features were found to appear in ρ' with increasing Prandtl number; this result can be observed in Fig. 6. The temporal evolution of the density perturbation field is visualized using ρ_{rms} in Fig. 7. The Pr=7 case has significantly stronger fluctuations than the Pr=0.2 case and they persist for much longer time. The ρ_{rms} field in the Pr=1 case is closer to the Pr=7 case than the Pr=0.2 case but shows reduced strength and lifespan of fluctuations due to the increased molecular diffusivity compared to the Pr=7 case.

The ρ_{rms} field can also be used to visualize the internal gravity waves that are radiated from the wake to the surroundings. From Fig. 7, one can observe that the Pr=7 case

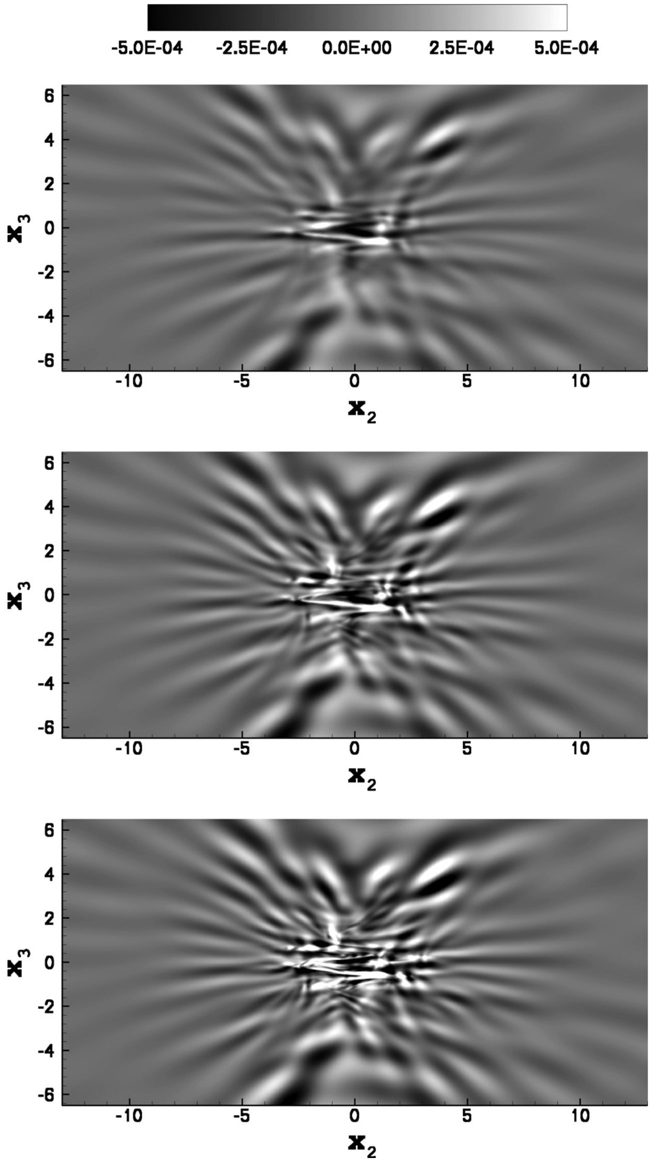

FIG. 6. Instantaneous ρ' at $t=90$ at the streamwise centerplane, $x_1=L_1/2$. Top Pr=0.2, middle Pr=1, bottom Pr=7.

exhibits stronger wave activity for longer time than the Pr=0.2 case. One can calculate the internal wave flux of the wake to verify this observation. Integrating the pressure transport around the boundaries of the domain gives a measure of the energy lost from the wake to the surroundings due to internal wave transport. The integrated wave flux is defined,

$$T_p = \int_C \langle p' u_n' \rangle dC,$$

where C is the boundary of the x_2-x_3 cross section of the computation domain and u_n' is the fluctuating velocity normal to C. The wave flux has a strong dependence on the Prandtl number, as shown in Fig. 8. Reduced wave flux with lower Prandtl number is reasonable since larger molecular diffusivity damps potential energy stored in the fluctuating density field more effectively, which results in less potential energy available to be transferred by buoyancy to kinetic energy in the NEQ regime.

It is desirable to have a measure of the energy associated with the wake. For this study we define the total wake energy as the sum of the mean kinetic energy, turbulent kinetic energy, and the turbulent potential energy using the following definition:

$$E = mke + K + K_\rho = \frac{1}{2}\langle u_i \rangle \langle u_i \rangle + \frac{1}{2}\langle u_i' u_i' \rangle + \frac{1}{2\ \mathrm{Fr}^2}\langle \rho'^2 \rangle, \tag{13}$$

where K_ρ is defined as done by Itsweire *et al.*[23] By integrating *mke*, K, and K_ρ over the computational domain, the net MKE, net TKE, and net TPE are obtained, respectively. As shown in Fig. 9(a), the integrated total wake energy was found to be behave qualitatively and quantitatively similar in the Pr=1 and Pr=7 cases. The Pr=0.2 case showed similar qualitative trends but a reduced quantitative value until very late time. The MKE (not shown) is similar among the three cases but TKE and TPE are reduced in the Pr=0.2 case. The reduced value of TKE obtained shows that the Prandtl number effect is not limited to the density field. It is interesting to note that reducing the Prandtl number by a factor of 5 has more of an effect on the turbulent kinetic and turbulent potential energy than increasing the Prandtl number by a factor of 7.

One-dimensional spectra are calculated in the periodic direction x_1 for the velocity and density fields to assess the spectral distribution of energy. To increase the sample size of the spectra, an $n_{\mathrm{spec}} \times n_{\mathrm{spec}}$ cross pattern is used, as shown in Fig. 10. The centerline point and its $(n_{\mathrm{spec}}-1)/2$ neighbors are averaged in the x_2 direction and then the centerline point and its $(n_{\mathrm{spec}}-1)/2$ points in the x_3 direction are averaged to determine spectra at the centerline. The cross pattern allows an average of $2n_{\mathrm{spec}}$ points to be used for spectra instead of a single point. A larger sample size reduces the statistical jitter. $n_{\mathrm{spec}}=11$ for the Pr=7 case, and $n_{\mathrm{spec}}=5$ for the Pr=0.2, Pr=1, and the latter part of the Pr=7 case. Less points were used for the coarser grid so that the spatial extent of the averaging was consistent between all the cases.

The higher Prandtl number simulations have more energy at the intermediate and small scales in both the velocity and density fields, as shown in Fig. 11. This relationship was observed in the early, intermediate, and far wake. Energy spectra are shown in Fig. 11 for both the turbulent kinetic energy and the turbulent potential energy. $E(k)$ and $E_\rho(k)$ are defined such that

$$K(x_{2,c},x_{3,c}) = \int_0^\infty E(k)dk, \quad K_\rho(x_{2,c},x_{3,c}) = \int_0^\infty E_\rho(k)dk,$$

where $x_{2,c}$ is the centerline in x_2 and $x_{3,c}$ is the centerline in x_3. The centerline values are used because they are the most energetic part of the wake.

It is known that for a passive scalar, increasing or decreasing the Prandtl number will change the length scale at which the dissipative subrange begins.[1] Increasing Prandtl number shifts the dissipation subrange for $E_\rho(k)$ to smaller scales, whereas decreasing Pr shifts the dissipation subrange

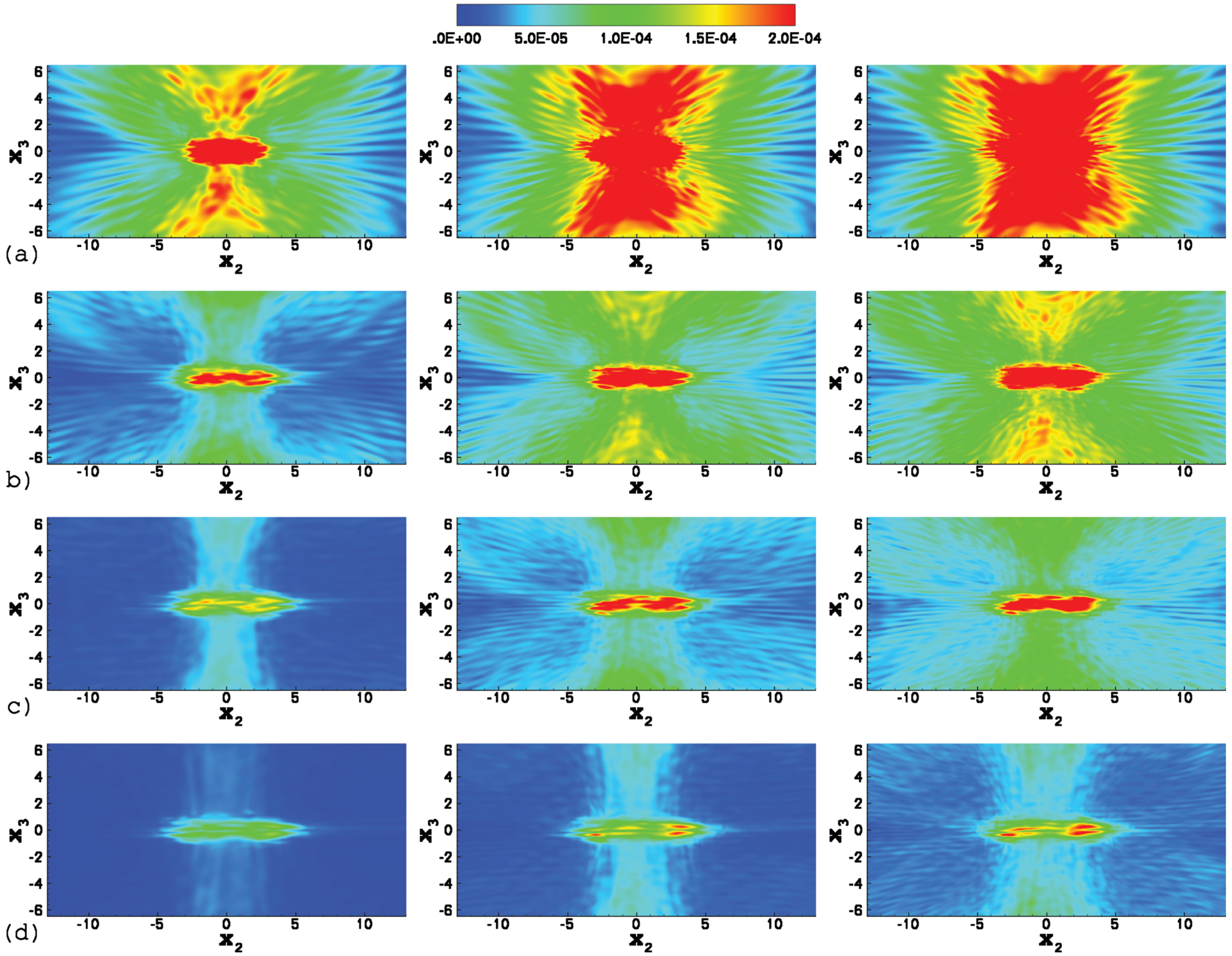

FIG. 7. (Color) ρ_{rms} evolution. Left column Pr=0.2, middle column Pr=1, right column Pr=7. (a) $t=90$. (b) $t=150$. (c) $t=210$. (d) $t=300$.

to larger scales. If the density were a passive scalar then we would not expect to observe any differences in $E(k)$. This is not the case which further illustrates that ρ should not be considered a passive scalar. While ρ is an active scalar, the argument made for a passive scalar concerning the relative locations of the dissipation subrange for $E(k)$ and $E_{\rho}(k)$ at large or small Prandtl number is applicable for the current study. Figure 11(a) confirms the increase in extent of the inertial subrange for $E_{\rho}(k)$ with higher Prandtl numbers but there does not appear to be a viscous-convective subrange as predicted for a passive scalar.[1]

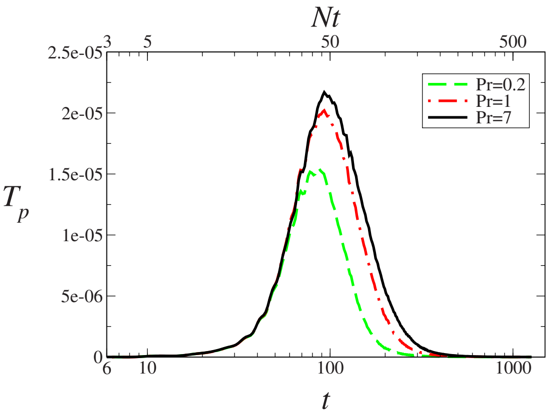

FIG. 8. (Color online) Integrated wave flux evolution.

Compensated spectra can be used to assess whether or not Kolmogorov scaling is present, plots are given in Figs. 11(c) and 11(d) for $E_{\rho}(k)$ and $E(k)$, respectively. It is interesting to note that the $E_{\rho}(k)$ plot for Pr=7 approximately shows Kolmogorov scaling $k^{-5/3}$ over a decade at early times. There is a shorter $k^{-5/3}$ range at intermediate and late times as well. Approximately $k^{-5/3}$ inertial scaling is observed at very early time in the $E(k)$ spectrum but this scaling is not maintained in the intermediate or far wake. In contrast, the $E_{\rho}(k)$ spectrum has a short range with approximately $k^{-5/3}$ inertial scaling even at $t=1000$.

If we return to Figs. 11(a) and 11(b) and include the spectra for the Pr=1 case while focusing in on time $t=20$, we can observe that both the $E(k)$ spectrum and the $E_{\rho}(k)$ spectrum for Pr=1 resemble Pr=7 more closely than Pr=0.2. This is shown in Fig. 12. The Pr=0.2 case shows a shorter inertial range and reduced energy at wavenumbers greater

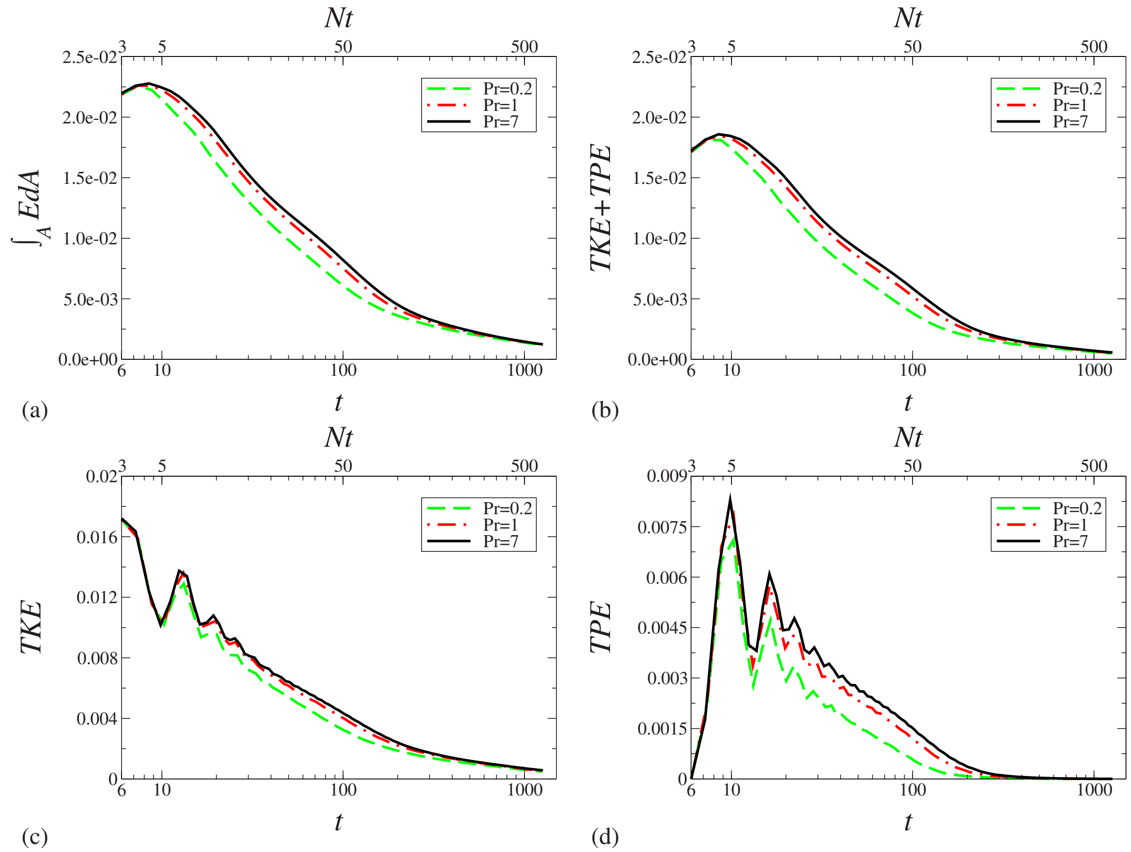

FIG. 9. (Color online) (a) Total energy evolution. (b) Turbulent energy evolution. (c) Turbulent kinetic energy evolution. (d) Turbulent potential energy evolution. Note that all plots show integrated quantities.

than $k=60$. The larger scales in the Pr=0.2 case are being interfered with by diffusive effects. The reduced energy in the Pr=0.2 case is similar to the behavior of a lower Re flow. The value of RePr=10 000×0.2=2000 is rather small in the Pr=0.2 case and, therefore, the lower wavenumbers (larger scales) are directly affected by molecular diffusion. These differences in the spectra are responsible for the larger impact on T_p, K, and K_ρ from reducing Pr with respect to Pr =1 by a factor of 5 than increasing Pr by a factor of 7.

If one examines the three components of $E(k)$ for the Pr=7 case shown in Fig. 13(a), one can observe that, at large scales, $E(k)$ is dominated by $E_{11}(k)$ and $E_{22}(K)$. For small scales $E_{33}(k)$ dominates $E(k)$. The dominance of $E_{33}(k)$ at small scales is reasonable as the density fluctuations at small scales lead to fluctuations in the vertical velocity. The opposite behavior with respect to the relative importance of $E_{33}(k)$ to $E(k)$ occurs for the Pr=0.2 case shown in Fig. 13(b).

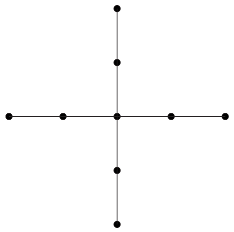

FIG. 10. Cross pattern used for calculating spectra.

Scalar dissipation is the main sink for turbulent potential energy stored in the density field. The scalar dissipation varies strongly with the Prandtl number. This is to be expected from the role of Pr in the definition of scalar dissipation,

$$\varepsilon_\rho = \frac{1}{\mathrm{Pr}\ \ \mathrm{Re}\ \ \mathrm{Fr}^2}\left\langle \frac{\partial \rho'}{\partial x_k}\frac{\partial \rho'}{\partial x_k}\right\rangle .$$

However, as shown in Fig. 14(d) ε_ρ does not scale as 1/Pr because the density perturbation gradients are different in the three cases. Density fluctuation gradients are larger in the higher Pr cases but not so large as to overcome the 1/Pr factor in the definition of ε_ρ.

Analogous to the role of scalar dissipation for the turbulent potential energy, turbulent dissipation is the main sink of turbulent kinetic energy. The turbulent dissipation is defined as follows:

$$\varepsilon = \frac{1}{\mathrm{Re}}\left\langle \frac{\partial u_i'}{\partial x_k}\frac{\partial u_i'}{\partial x_k}\right\rangle .$$

Note that formally this is the definition of the pseudodissipation, however this is often used as it is essentially identical to the dissipation in high-Re turbulence.[24] Significantly stronger turbulent dissipation occurs in the Pr=7 case than the Pr=1 and Pr=0.2 cases. The trend of increasing turbulent dissipation with increasing Prandtl number can be clearly observed from $\int_A \varepsilon dA$ in Fig. 14(b). The change in turbulent dissipation is consistent with the fact that density is not a

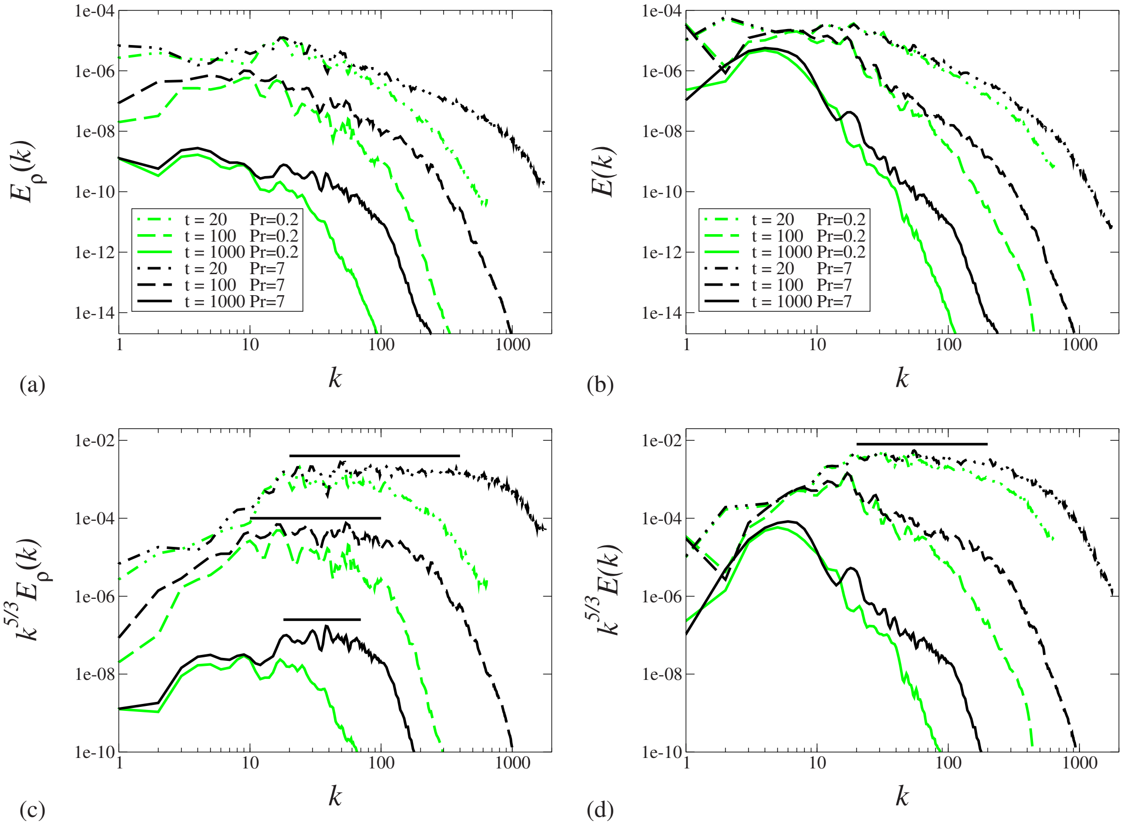

FIG. 11. (Color online) Differences between spectra in the Pr=0.2 and Pr=7 cases illustrated at three times, $t=20,100,1000$. (a) $E_\rho(k)$. (b) $E(k)$. (c) Compensated spectra for $E_\rho(k)$; see (a) for legend. (d) Compensated spectra for $E(k)$; see (b) for legend. The horizontal black lines in (c) and (d) show the range of wavenumbers where Kolmogorov scaling is present for the Pr=7 case. Note that a 5 point weighted average is used for the first 60 modes and an 11 point unweighted average is used for $k>60$.

passive scalar. The result of increasing ε and decreasing ε_ρ with increasing Pr shown in Figs. 14(a) and 14(b) agrees with the results of Gerz, Schumann, and Elghobashi.[8]

The quantity $\varepsilon+\varepsilon_\rho$ represents the net dissipation of the turbulent energy, $K+K_\rho$; $\int_A(\varepsilon+\varepsilon_\rho)dA$ is shown in Fig. 14(c). The net dissipation is much larger in the Pr=0.2 case which is consistent with the reduced TKE+TPE shown in Fig. 9. The Pr=7 and Pr=1 cases exhibit comparable values of net dissipation with the Pr=7 case having slightly larger net dissipation after $t>10$.

Following previous studies,[12,15,25] the mixing efficiency can be defined using ε_ρ and ε. To ensure that the mixing efficiency takes values between 0 and 1, the normalizing definition

$$\gamma_d=\frac{\int_A \varepsilon_\rho\, dA}{\int_A \varepsilon\, dA+\int_A \varepsilon_\rho\, dA}$$

was used. The physical meaning of this definition is that efficiency is defined as the fractional contribution of molecular mixing of turbulent potential energy to molecular mixing of total fluctuation energy. As the disturbances to the back-

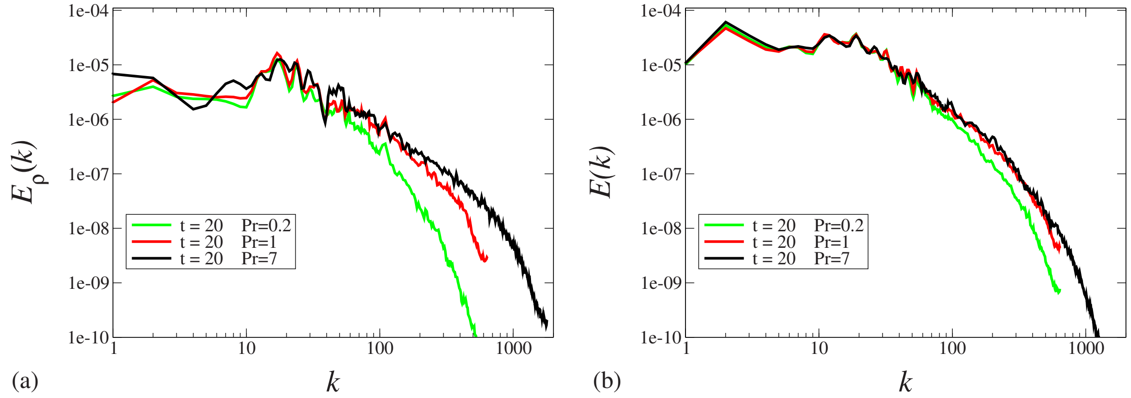

FIG. 12. (Color online) Separation in scales at different values of Pr. (a) $E_\rho(k)$. (b) $E(k)$.

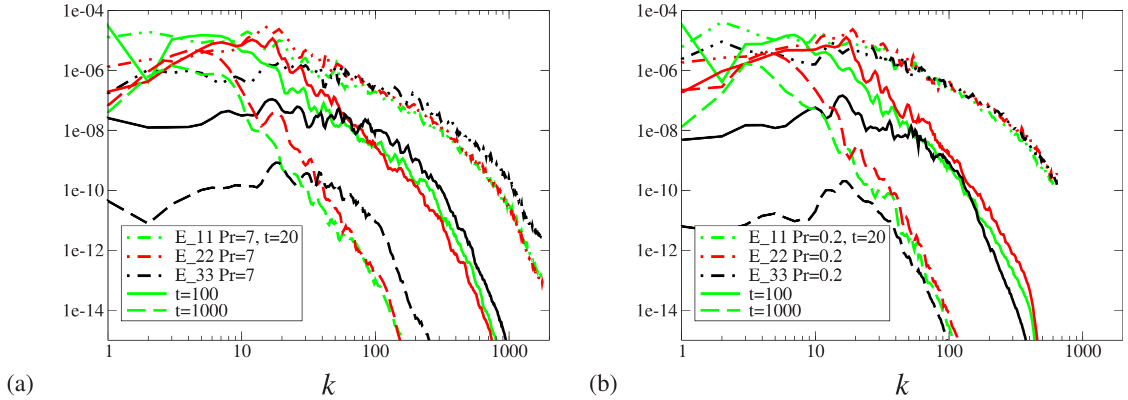

(a) (b)

FIG. 13. (Color online) (a) Components of $E(k)$ for the Pr=7 case. (b) Components of $E(k)$ for the Pr=0.2 case. Note that a 5 point weighted average is used for the first 60 modes and an 11 point unweighted average is used for $k>60$.

ground density field are small, one can get a picture of how well-mixed the wake is by examining $\rho_{\rm rms}$ in Fig. 7. Consistent with the contour plots of $\rho_{\rm rms}$, γ_d was found to be significantly higher with decreasing Prandtl number; this is shown in Fig. 15. The trend of decreased mixing efficiency with increasing Prandtl number found by Smyth, Moum, and Caldwell[12] and Brucker and Sarkar[15] in their studies on shear layers is found to hold in the turbulent stratified wake as well.

The mixing efficiency tends to zero at late times because the mean flow excites stronger velocity fluctuations in the horizontal plane than density fluctuations and, consequently, the flow becomes quasi-two-dimensional at late time and density fluctuations become weaker since vertical motion is required to obtain ρ' whereas $u_{i,\rm rms}$ can occur in-plane. Figure 16 shows the dominance of fluctuations in the horizontal plane at late time in the Q2D region. Figure 16(a) shows the ratio of the integrated $\rho_{\rm rms}$ and integrated $u_{h,\rm rms}$, where $u_{h,\rm rms}=(u_{1,\rm rms}^2+u_{2,\rm rms}^2)^2$. Note that $\rho_{\rm rms}$ is scaled by 1/Fr for dimensional consistency. Figure 16(a) also shows the ratio of

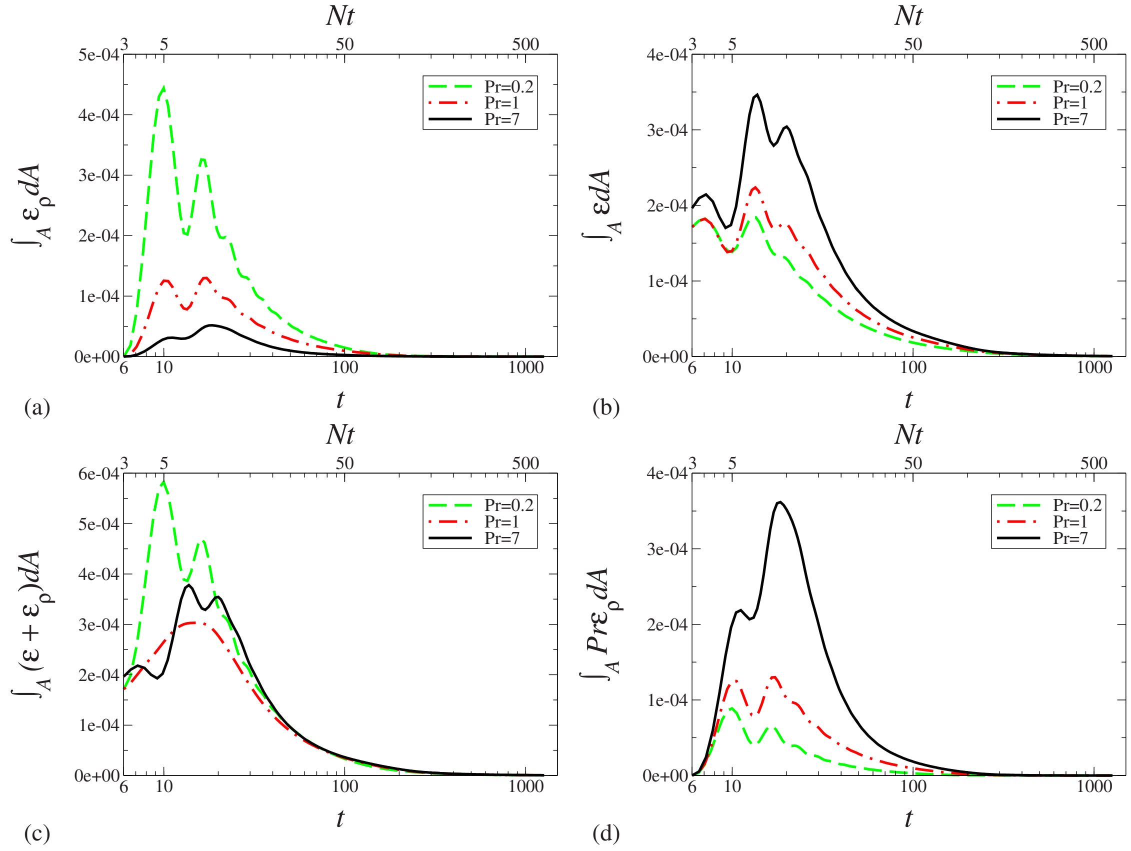

(a) (b) (c) (d)

FIG. 14. (Color online) Dissipation evolution. (a) Integrated dissipation of K. (b) Integrated dissipation of K_ρ. (c) Integrated dissipation of $K+K_\rho$. (d) Integrated dissipation of K_ρ with Prandtl number explicit dependence removed. The initial difference in $\int_A \varepsilon(t=6)dA$ between the Pr=7 and Pr=0.2, 1 cases is due to the interpolation used to generate the initial conditions. Information from gradients is lost upon transfer from a fine grid to a coarse grid.

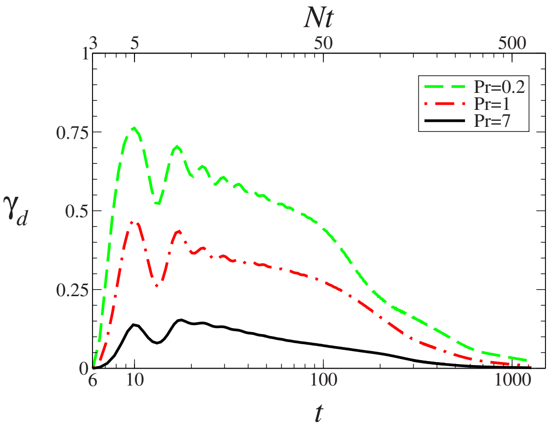

FIG. 15. (Color online) Mixing efficiency based on γ_d.

integrated $u_{3,\mathrm{rms}}$ and $u_{h,\mathrm{rms}}$. Both quantities go to zero at late time. A local Froude number was defined using $\mathrm{Fr}_h = U_0/(2R_2N)$, this value also goes to zero as shown in Fig. 16(b).

The buoyancy flux term quantifies the transfer of energy between the turbulent potential energy and turbulent kinetic energy; it is defined as

$$B = -\frac{1}{\mathrm{Fr}^2}\langle \rho' u_3' \rangle.$$

As shown in Fig. 17, the buoyancy flux shows a bias depending on the magnitude of the Prandtl number. For Pr=1, $\int_A B dA$ is approximately centered around zero for $t > 350$. For Pr=1, there is an initial transient followed by a peak in $\int_A B dA$ at $t \approx 90$ followed by a smooth decay down to zero. For Pr=7, $\int_A B dA$ shows a positive bias and for Pr=0.2, $\int_A B dA$ shows a negative bias. Between $t \approx 30$ and $t \approx 80$ the magnitude of $\int_A B dA$ for the Pr=7 and Pr=0.2 cases is comparable, this also holds from $300 \leq t \leq 600$. Between $80 \leq t \leq 300$ the magnitude of $\int_A B dA$ is much larger for the Pr=7 case than the Pr=0.2 case.

At very late time, $t \gtrsim 600$, the magnitude of $\int_A B dA$ is much larger in the Pr=0.2 case than the Pr=7 case. A positive value of B will result in more energy being transferred from turbulent potential to turbulent kinetic energy. In contrast, a negative buoyancy flux results in energy moving from turbulent kinetic to turbulent potential energy. At lower Prandtl numbers, molecular diffusion is an effective smoother, quickly damping out density differences and reducing the turbulent potential energy. This causes energy to be transferred on average from turbulent kinetic to turbulent potential energy. Conversely, for high Pr the viscous diffusion acts on the velocity field reducing the turbulent kinetic energy while the reduced molecular diffusivity allows for more energy storage in the form of turbulent potential energy. It is the coupling between the vertical velocity and density field which allows the energy to be transferred between potential and kinetic modes. The average rate of energy transfer is from the higher energy modes to lower energy modes.

The mixing efficiency is often quantified using

$$\gamma = \frac{\int_A B dA}{\int_A B dA + \int_A \varepsilon dA}$$

for stratified turbulent flows. The preceding definition is not appropriate for turbulent stratified wakes because the value of $\int_A B dA$ oscillates frequently between positive and negative values which results in γ not being positive definite. Another problem is that $\int_A B dA$ and $\int_A \varepsilon dA$ are of the same order which makes it possible to obtain unreasonably large values of γ when the magnitudes of $\int_A B dA$ and $\int_A \varepsilon dA$ are comparable but their signs are opposite.

IV. CONCLUSIONS

DNS at Re=10 000, Fr=2, and $\mathrm{Pr} \epsilon [0.2, 1, 7]$ was performed to examine the effect of the Prandtl number on a turbulent wake in a stratified fluid. Bulk quantities such as wake defect velocity and the wake dimensions were found to be weakly influenced by the Prandtl number. However, the Prandtl number was found to strongly affect the density perturbation field. Through the coupling between kinetic and potential energy, differences in the density perturbation field resulted in differences in the wave flux, total energy of the wake, turbulent and scalar dissipation, spectral distribution of energy in the density and velocity fields, mixing efficiency, and buoyancy flux. For example, the maximum inter-

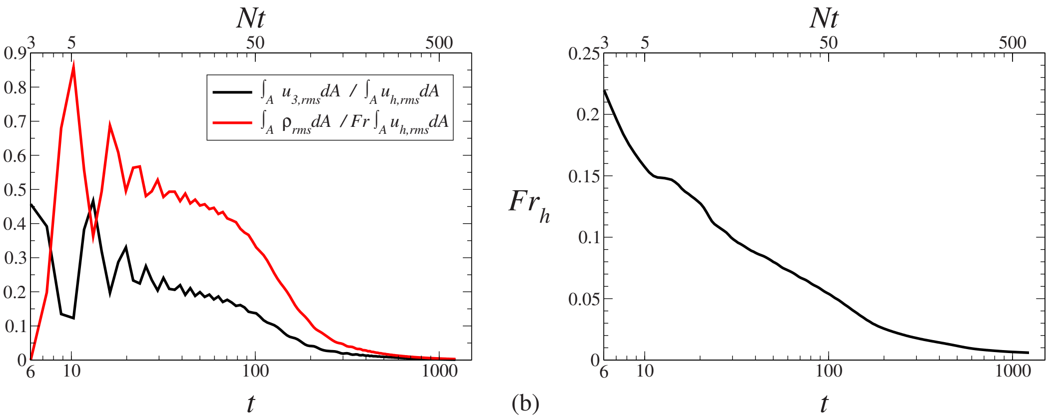

(a) (b)

FIG. 16. (Color online) (a) Fluctuation strength. (b) Local horizontal Froude number. Both plots show data from the Pr=1 case, the same trends occur in all three cases.

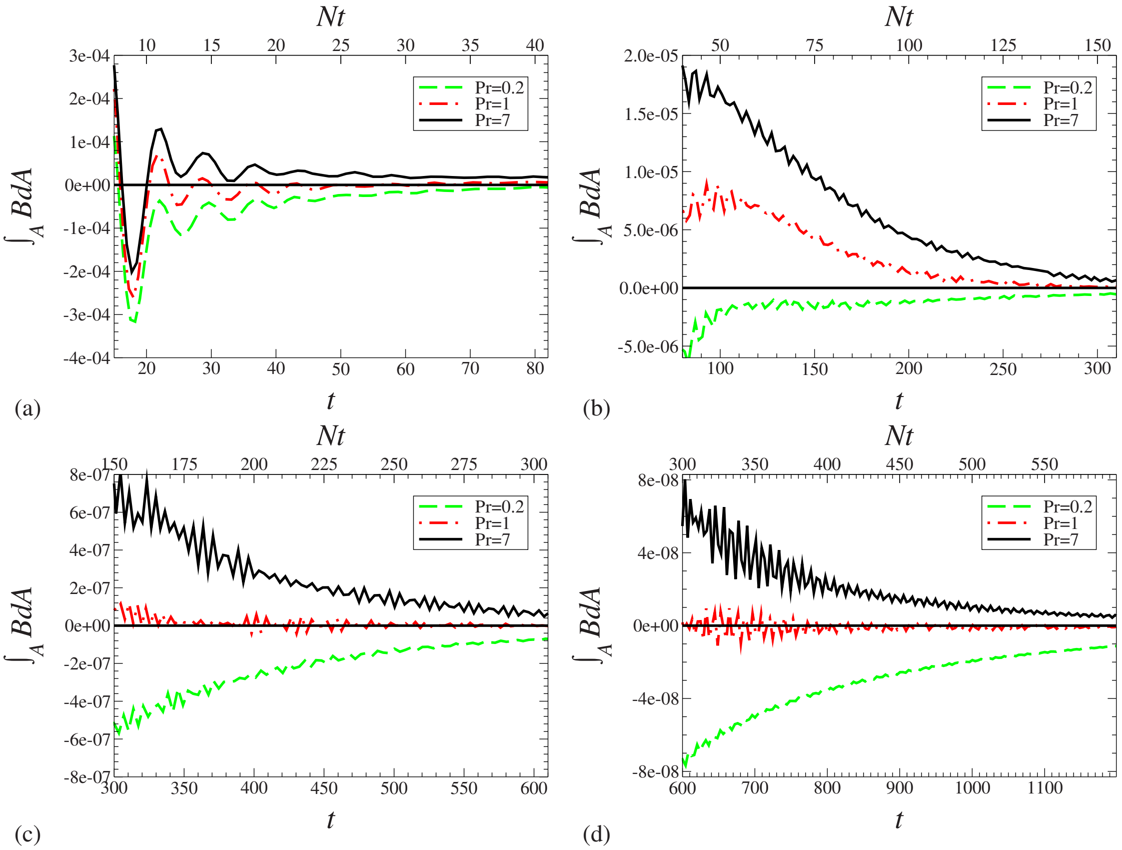

FIG. 17. (Color online) Buoyancy flux bias. (a) Early time. (b) Intermediate time. (c) Late time. (d) Very late time. Note that a 15 point running average was used to filter the raw data to clearly show the bias based on Pr.

nal wave flux at Pr=7 exceeds that at Pr=0.2 by about 50%. The Pr=7 case shows a decade of wavenumbers with approximately $k^{-5/3}$ inertial scaling in both density and velocity spectra at early time. A short $k^{-5/3}$ range is present at late time in the density field but not in the velocity for the Pr =7 case; none exists for the Pr=0.2 case. The Pr=7 case exhibits significantly higher values of ε and significantly lower values of ε_ρ compared to the Pr=0.2 case. The increased ε with increasing Pr clearly shows that density should not be treated as a passive scalar.

The degree of difference between the Pr=1 case and the other cases varied based on whether the Prandtl number was increased or decreased. In general, differences were more pronounced between the Pr=1 and Pr=0.2 cases than the Pr=1 and Pr=7 cases. This is because the value of RePr =2000 in the Pr=0.2 case is rather small so that direct damping by molecular diffusivity extends to the larger scales. Lower values of Pr damp density fluctuations more efficiently which results in substantial differences in several of the quantities used to characterize the turbulent wake, this effect can be seen most clearly by examining the spectra of $E(k)$ and $E_\rho(k)$ as shown in Fig. 12. At higher values of Pr there are differences in wake quantities but they tend to be small-scale features which do not have a significant impact on the larger scale features of the wake.

The main question this paper sought to answer, “Is it reasonable to assume Pr=1 for conducting simulations of submersible wakes in a stratified environment with Pr=7?” has been answered in the affirmative. The qualitative agreement between the mean flow and second-order turbulent statistics in the Pr=1 and Pr=7 cases is very good. While quantitative differences do exist between the Pr=1 and Pr=7 cases, the differences are small relative to the significantly higher computational cost required by increased resolution. As the upper limit of the Reynolds number for stratified turbulent wake simulations using DNS is still substantially below that in applications, it is more important to increase the Reynolds number to a more realistic value as it has a significant impact on the wake dynamics.[2,26]

ACKNOWLEDGMENTS

S.S. and K.A.B. are pleased to acknowledge support from the Office of Naval Research (ONR) Grant No. N00014-07-10133, program monitor Ron Joslin. M.B.S. received support on this project from an NDSEG Fellowship (HPCMO) and a Jacobs School Fellowship (UCSD). This research was made with Government support under and awarded by DoD, Air Force Office of Scientific Research, National Defense Science and Engineering Graduate (NDSEG) Fellowship, 32 CFR 168a. Computational resources were provided by the Department of Defense High Performance Computing Modernization program. All simulations were run on Jade, a Cray XT4 at the U.S. Army Corps of Engineers Engineering Research and Development Center.

[1] H. Tennekes and J. L. Lumley, *A First Course in Turbulence* (MIT, Cambridge, MA, 1972).
[2] K. A. Brucker and S. Sarkar, "A comparative study of self-propelled and towed wakes in a stratified fluid," J. Fluid Mech. **652**, 373 (2010).
[3] J. T. Lin and Y. H. Pao, "Wakes in stratified fluids," Annu. Rev. Fluid Mech. **11**, 317 (1979).
[4] G. R. Spedding, "The evolution of initially turbulent bluff-body wakes at high internal Froude number," J. Fluid Mech. **337**, 283 (1997).
[5] M. Bonnier and O. Eiff, "Experimental investigation of the collapse of a turbulent wake in a stably stratified fluid," Phys. Fluids **14**, 791 (2002).
[6] M. J. Gourlay, S. C. Arendt, D. C. Fritts, and J. Werne, "Numerical modeling of initially turbulent wakes with net momentum," Phys. Fluids **13**, 3783 (2001).
[7] D. G. Dommermuth, J. W. Rottman, G. E. Innis, and E. A. Novikov, "Numerical simulation of the wake of a towed sphere in a weakly stratified fluid," J. Fluid Mech. **473**, 83 (2002).
[8] T. Gerz, U. Schumann, and S. E. Elghobashi, "Direct numerical simulation of stratified homogeneous turbulent shear flows," J. Fluid Mech. **200**, 563 (1989).
[9] T. Gerz and H. Yamazaki, "Direct numerical simulation of buoyancy-driven turbulence in stably stratified fluid," J. Fluid Mech. **249**, 415 (1993).
[10] T. Gerz and U. Schumann, "A possible explanation of countergradient fluxes in homogeneous turbulence," Theor. Comput. Fluid Dyn. **8**, 169 (1996).
[11] W. D. Smyth and J. N. Moum, "Anisotropy of turbulence in stably stratified mixing layers," Phys. Fluids **12**, 1343 (2000).
[12] W. D. Smyth, J. N. Moum, and D. R. Caldwell, "The efficiency of mixing in turbulent patches: Inferences from direct simulations and microstructure observations," J. Phys. Oceanogr. **31**, 1969 (2001).
[13] L. Wang and X. Y. Lu, "Large eddy simulation of stably stratified turbulent open channel flows with low- to high-Prandtl number," Int. J. Heat Mass Transfer **48**, 1883 (2005).
[14] J. H. Lienhard and C. W. Van Atta, "The decay of turbulence in thermally stratified flow," J. Fluid Mech. **210**, 57 (1990).
[15] K. A. Brucker and S. Sarkar, "Evolution of an initially turbulent stratified shear layer," Phys. Fluids **19**, 105105 (2007).
[16] S. Basak, "Dynamics of stratified shear layers with horizontal shear," Ph.D. thesis, University of California San Diego, 2005.
[17] S. Basak and S. Sarkar, "Dynamics of a stratified shear layer with horizontal shear," J. Fluid Mech. **568**, 19 (2006).
[18] J. H. Williamson, "Low-storage Runge–Kutta schemes," J. Comput. Phys. **35**, 48 (1980).
[19] T. R. Bewley, "Optimal and robust control and estimation of transition, convection, and turbulence," Ph.D. thesis, Stanford University, 1999.
[20] J. J. Riley and S. M. de Bruyn Kops, "Dynamics of turbulence strongly influenced by buoyancy," Phys. Fluids **15**, 2047 (2003).
[21] P. M. Bevilaqua and P. S. Lykoudis, "Turbulence memory in self-preserving wakes," J. Fluid Mech. **89**, 589 (1978).
[22] P. Moin and K. Mahesh, "Direct numerical simulation: A tool in turbulence research," Annu. Rev. Fluid Mech. **30**, 539 (1998).
[23] C. E. Itsweire, J. R. Koseff, D. A. Briggs, and J. H. Ferziger, "Turbulence in stratified shear flows: Implications for interpreting shear-induced mixing in the ocean," J. Phys. Oceanogr. **23**, 1508 (1993).
[24] S. B. Pope, *Turbulent Flows*, 1st ed. (Cambridge University Press, Cambridge, UK, 2000).
[25] W. R. Peltier and C. P. Caulfield, "Mixing efficiency in stratified shear flows," Annu. Rev. Fluid Mech. **35**, 135 (2003).
[26] P. J. Diamessis and G. R. Spedding, "Scaling and structure of turbulent wakes at high Reynolds number," in *Proceedings of the Sixth International Symposium on Stratified Flows*, edited by G. Ivey (University of Western Australia, Perth, Australia, 2006).